www.MaterialsViews.com

ADVANCED
ENERGY
MATERIALS

www.advenergymat.de

COMMUNICATION

Ionic Liquid Control Crystal Growth to Enhance Planar Perovskite Solar Cells Efficiency

Ji-Youn Seo, Taisuke Matsui, Jingshan Luo, Juan-Pablo Correa-Baena, Fabrizio Giordano, Michael Saliba, Kurt Schenk, Amita Ummadisingu, Konrad Domanski, Mahboubeh Hadadian, Anders Hagfeldt, Shaik M. Zakeeruddin, Ullrich Steiner, Michael Grätzel, and Antonio Abate*

Perovskite solar cells (PSCs) have had a lasting impression on the scientific community because of their fast progress as high efficient and low cost technology. Starting from the seminal work of Kojima et al. in 2009, in only seven years power conversion efficiencies above 22% have already been reported and certified.[1–4] In aspect of economic and technological analysis, one promising route to industrialization of PSCs is to take advantage of the complementary band gaps of perovskite and silicon solar cells, i.e., to create a perovskite-silicon tandem. In a tandem architecture the perovskite can be deposited on the top of bottom cell to potentially overtake the Shockley Queisser limitation for a single junction device.[5] This strategy is promising, but it requires low-temperature processing (100 °C) to avoid damaging of the bottom silicon cell. Currently, the highest efficient PSCs employ a mesoscopic TiO$_2$ electron contact, which is processed at temperature above

J.-Y. Seo, Dr. J. Luo, Dr. F. Giordano, Dr. M. Saliba,
A. Ummadisingu, K. Domanski, Dr. S. M. Zakeeruddin,
Prof. M. Grätzel, Dr. A. Abate
Swiss Federal Institute of Technology (EPFL)
Laboratory of Photonics and Interfaces
Station 6, CH-1015 Lausanne, Switzerland
E-mail: antonio.abate@epfl.ch,
antonioabate83@gmail.com
T. Matsui
Advanced Research Division
Materials Research Laboratory
Panasonic Corporation
1006 Kadoma, Kadoma City, Osaka 571-8501, Japan
Dr. J.-P. Correa-Baena, M. Hadadian, Prof. A. Hagfeldt
Laboratory of Photomolecular Science
Institute of Chemical Sciences and Engineering
École Polytechnique Fédérale de Lausanne
CH-1015 Lausanne, Switzerland
Dr. K. Schenk
Institut des Sciences et Ingénierie Chimiques
Institut de Physique des Systèmes Biologiques
École Polytechnique Fédérale de Lausanne
CH-1015 Lausanne, Switzerland
M. Hadadian
Department of Chemistry
Ferdowsi University of Mashhad
Mashhad 91779, Iran
Prof. U. Steiner, Dr. A. Abate
Adolphe Merkle Institute
University of Fribourg
Chemin des Verdiers 4, CH-1700 Fribourg, Switzerland

400 °C and thus not compatible with the preparation of tandem devices. Although there are strategies to prepare mesoscopic TiO$_2$ at low temperature, the easiest approach would be to use a planar perovskite device without mesoporous layer.[6] We recently demonstrated low temperature processed SnO$_2$ as electron contact in planar PSCs for tandem silicon-perovskite solar cell.[7] Although the efficiency of our tandem device was one of the highest reported, the top planar PSC was poorly performing compared to a mesoscopic TiO$_2$-based device. Therefore, to profit from using perovskite in tandem with other photovoltaic materials, planar devices need to be improved.

In planar PSCs, the crystallinity, morphology, thickness, and surface coverage of perovskite film are critical for the device performance.[8] Several methods have been proposed to prepare high-quality perovskite layer, such as spin-coating, two-step sequential deposition, and vacuum vapor deposition.[3,9–12] Even though the one-step spin-coating method enabled among the highest efficiencies, the perovskite films frequently showed poor surface coverage, which resulted in a reduced cell performance.[13] To overcome these issues, control of perovskite crystal growth and morphology has been widely investigated using several additives in the perovskite precursor solution.[14–16] Shahiduzzaman et al. made use of the low vapor pressure ionic liquid (IL) 1-hexyl-3-methylimidazolium chloride to control the film morphology by forming a uniform distribution of perovskite nanoparticles.[16] Moore et al. demonstrated that methylammonium formate can be used as an additive to produce higher quality, crystalline perovskite films.[15] Although these studies suggested that adding ILs in the perovskite precursor solution may help to prepare better solar cells, there are currently no reports that implemented this strategy to improve state-of-the-art planar PSCs.

In this work, we demonstrate that ionic liquids enable the highest ever reported stabilized power conversion efficiency for a planar perovskite solar cell. We show that compact perovskite films with larger crystalline domain can be prepared from solution by adding particular ionic liquids, such as methylammonium formate, to the precursors. We demonstrate that larger crystalline domains result is a more effective charge collection and thus better photovoltaic performances. We propose an IL-driven mechanism of crystallization as a new strategy to prepare high-efficiency planar perovskite solar cell.

ILs are well known for their extremely low vapor pressure, which makes them nonvolatile liquids. If added in small
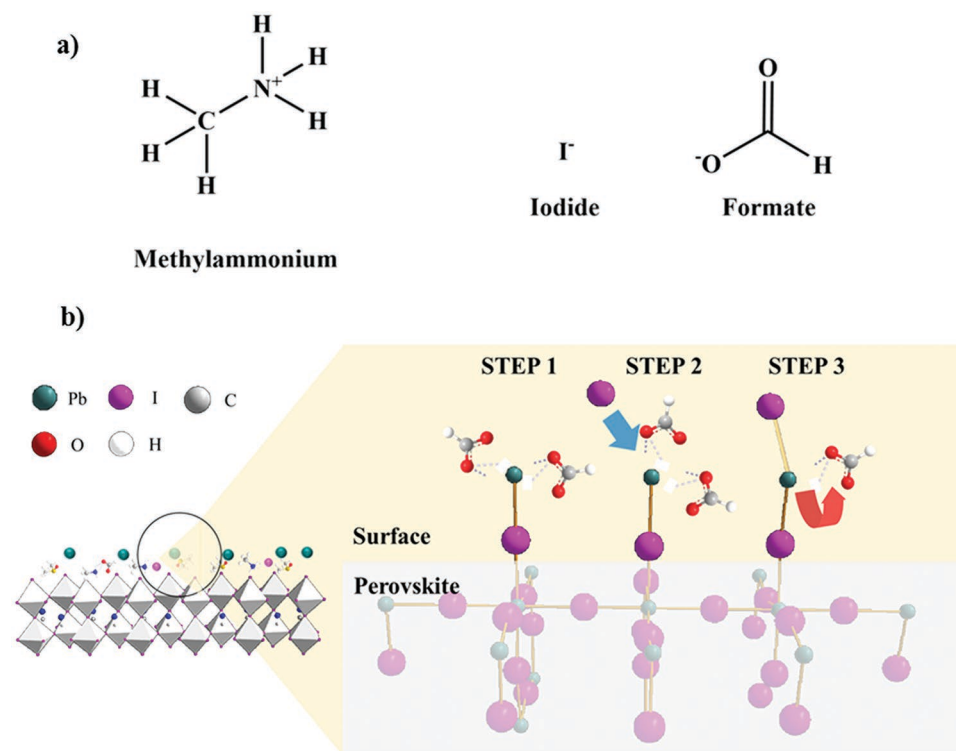
COMMUNICATION

Figure 1. a) Molecular structure of the organic precursors methylammonium iodide and formate. b) Schematic of the proposed perovskite crystal growth mechanism as controlled by the formate anions.

amount (few mol%) in the precursor solution, they remain in the perovskite film after all the solvent has evaporated during the annealing.[15,16] For this study we focused on the IL methylammonium formate (MAF), owing to its affinity with the perovskite precursor methylammonium iodide (MAI), which is selected after screening morphology changes of perovskite films with other affinities including methylammonium chloride (see the Supporting Information).[17] The chemical structures of MAF and MAI are shown in **Figure 1**a. They have the same cation (methylammonium) and a different counter anion, formate (HCOO−) or iodide (I−). Since HCOO− is known to form metal-organic complex with Pb2+, our working hypothesis was that the HCOO− influences the crystal growth of the perovskite interacting with Pb2+.[18] In Figure 1b, we depict a schematic view of the proposed mechanism: STEP (1) HCOO− coordinates with Pb^{2+} in solution and during the early stage of the crystal growth; STEP (2) the complex HCOO−-Pb+ is gradually displaced by Pb+-I− when films are heated to 100 °C; STEP (3) HCOO−-Pb+ coordination is completely replaced by Pb+-I− enabling the crystal growth. Once the crystallization is completed MAF sits at the surface of the perovskite crystals as schematically presented in the left hand side of Figure 1b.

To investigate the impact of the MAF on the crystal growth, we prepared perovskite precursor solutions with and without 5 mol% of MAF. Perovskite films were prepared on SnO_2 deposited fluorine-doped tin oxide (FTO) substrates by spin coating the precursor solution in a nitrogen filled glovebox using the one-step antisolvent method.[19] In **Figure 2**a we report the pictures of the perovskite films collected every 5 s after placing the substrates on a hotplate at 100 °C. It is evident

that the film without MAF turns black earlier than the film with MAF. This simple experiment suggested that the crystal growth is slowed down by the presence of MAF. To look at the impact of the slower crystal growth on the film morphology, we collected scanning electron microscopy (SEM) images of the film surface after the annealing was completed (1 h at 100 °C). SEM images of perovskite films show that the average grain sizes are 170 and 325 nm without and with MAF, respectively. Therefore, a slower crystal growth induced larger average grain size. More interesting, we notice that the MAF inhibits the formation of grains smaller than 150 nm, which represent a great portion of the size distribution in the film without the MAF (see statistical distribution in Figure 2b).

In order to investigate the impact of the MAF on the crystal structure of the perovskite, X-ray diffraction (XRD) patterns were collected from perovskite films with and without MAF on SnO_2 substrates. The XRD spectra in **Figure 3**a show that the MAF-mediated perovskite is rather similar to the non-MAF film. This indicates that the HCOO− does not induce polymorphism or variation of the crystal lattice, even if it has a large influence on the perovskite film morphology, as shown in Figure 2. Furthermore, the fact that the diffraction pattern is the same, despite the size of HCOO− being larger than I− (HCOO− 249 Å > I− 220 Å), suggests that HCOO− is not incorporated in the perovskite crystal lattice.[17,20] It is interesting to note that the intensity of the peaks (112), (211), (202), and (224) relative to the intensity of the (110) peak (inset Figure 3a) is significantly larger in the film without MAF. Moreover, the full width at half maximum of the (110) peak is smaller with than without MAF (see the Supporting Information). These two
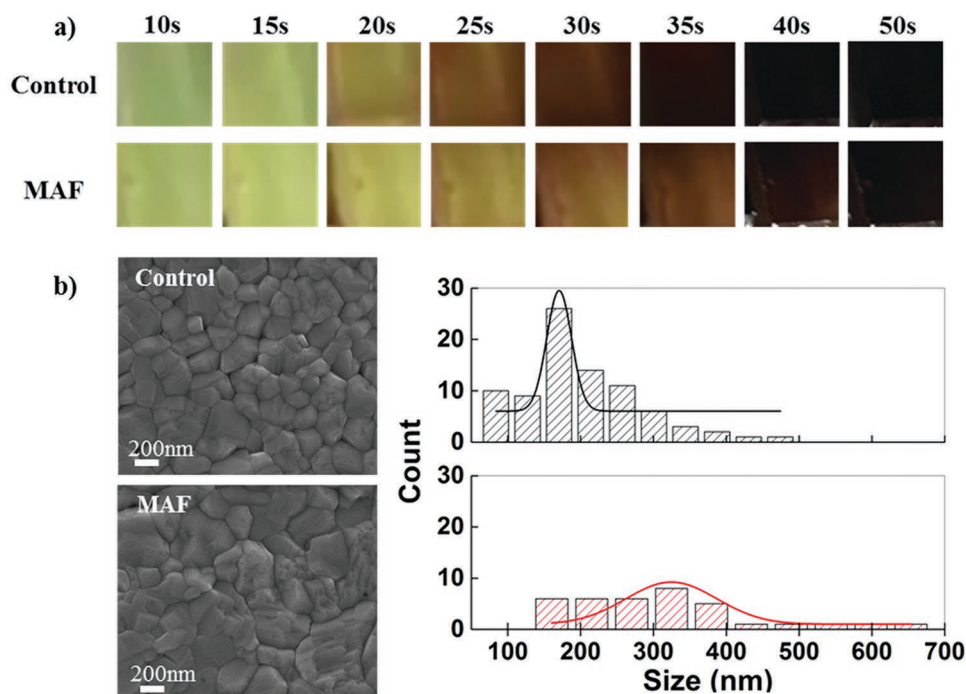
www.MaterialsViews.com

ADVANCED
ENERGY
MATERIALS
www.advenergymat.de

COMMUNICATION

Figure 2. Morphological analysis of the perovskite films with and without MAF. a) Pictures of perovskite films collected at subsequent delay times after posing the substrates on a hotplate at 100 °C. b) (left) Top-view SEM images of perovskite films after 1 h annealing at 100 °C. (right) Grain sizes distribution as estimated from the SEM images using Nano measurer 1.2 software.

data are compatible with a preferential crystal growth of (110) faces parallel to the substrate (see Figure 2b and the Supporting Information),[21] which is also supported by the change in morphology we observed with the SEM imaging.

PSCs with and without MAF in perovskite precursor solution were prepared on compact SnO_2, following the procedures
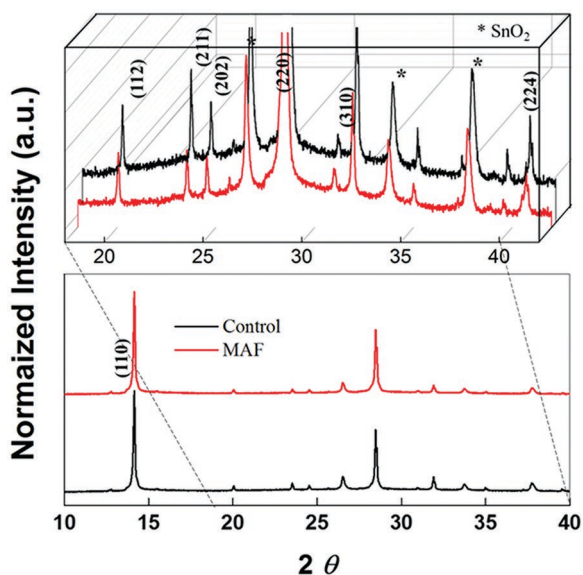

Figure 3. X-ray diffraction diagram of perovskite films deposited on SnO_2 substrates with and without MAF, the intensity is normalized to the peak at 14° (110). Inset: enlarged spectra displaying the relative intensities of the peaks between 18° and 42°.

previously reported by Baena et al.[22] **Figure 4**a displays the current density–voltage (J–V) curves of the best PSCs with the corresponding metrics reported in **Table 1**. The data show that MAF improves the short circuit current density (J_{sc}) by 1 mA cm^{-2}. This is confirmed by the incident photon-to-current efficiency (IPCE) in Figure 4b. We notice that with and without MAF the integrated current density is lower than what is measured from the J–V curves. This trend has been systematically observed also from other groups, and it can in part be attributed to a small spectral mismatch between the solar simulator and the standard AM 1.5 G emission.[19,23] In Figure 4c we reported the statistical analyses (box plot) of the maximum PCE collected from seven independent devices, which confirmed the improvement with MAF. To rule out the impact of the hysteresis on the estimated PCE, we tracked the device maximum power output for 5 min in order to extract the stabilized maximum PCE. Figure 4d displays that the PCE stabilizes after about 50 s to 18.9% for the control and 19.5% for MAF device (see Table 1), confirming the trend extracted from the J–V curves in Figure 4a. We want to highlight that our best control device matches the highest reported stabilized PCE for planar PSCs (≈19%).[24,25] Therefore, with MAF we are improving the state-of-the-art, reaching a new record for planar PSC with 19.5% stabilized PCE.

In order to investigate the origin of the improved performances with the MAF, we performed intensity-modulated photocurrent spectroscopy.[26] In **Figure 5**, we report the imaginary component frequency spectra of the current response to the light intensity-modulated (10% of the stationary value) around 100 mW cm^{-2} for devices with and without MAF. The spectra show three main features, which have been already
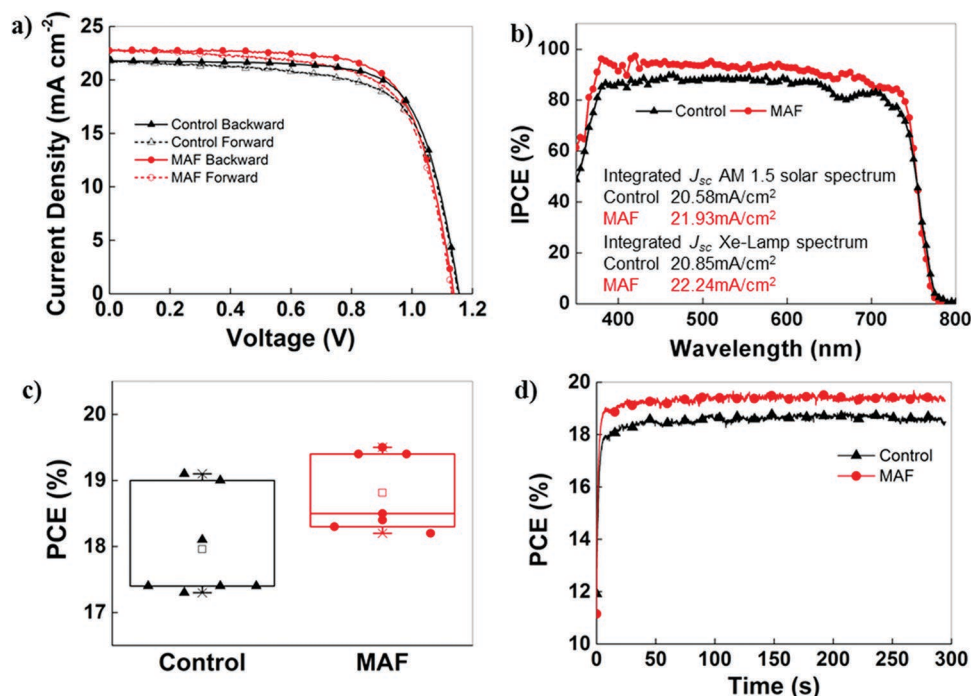
Figure 4. Photovoltaic metrics of perovskite solar cells prepared with and without MAF. a) J–V curves were measured from forward bias to short circuit condition and vice versa at the scan rate of 10 mV s⁻¹ under AM1.5 simulated solar light (94.8 mW cm⁻²). The device active area was defined using a black metal shadow mask with an aperture of 0.16 cm². b) Incident photon-to-current efficiency (IPCE) curves for the MAF and control device. c) Box plot of the PCE collected from seven devices. d) Maximum power conversion efficiency as function of time from the maximum power point tracking under AM1.5 simulated solar light.

reported by Baena et al. for similar planar PSCs.[27] The peak at low frequency (0.1 Hz–100 Hz) has been correlated to the resonant frequencies of the ions and ion vacancies migration within the perovskite lattice. Here, we note that the peak of the MAF device is shifted toward higher frequency, indicating a faster ion migration. This is in line with what was observed by Baena et al., who reported ions migrating faster in perovskite films composed of larger grains. Moving to higher frequency, there are two more peaks that have been assigned to the resonant frequencies of the charge dynamics within the perovskite and the other device components, such as the hole and the electron transporting layers. While the peak at highest frequency (fast charge dynamics) is rather similar with and without MAF, the peak at intermediated frequency (1–100 KHz) is clearly visible only in the control and almost vanishes in the MAF device.

As we have previously shown, this peak provides information on the slow charge transport dynamics within the device.[28] The fact that its intensity is significantly lower suggests that the slow charge transport pathways are inhibited by the MAF. This behavior correlates with the crystal size distribution we presented in Figure 2b, where we showed that MAF reduces the formation of grains smaller than 150 nm, while they represent a great portion of the size distribution in the film without the MAF. The cross-sectional SEM images (see Supporting Information) of a perovskite film with MAF shows that larger grains can cross the whole thickness of the perovskite film, thus forming a sort of local single crystalline devices. The charge transport through a single crystal is significantly faster than through the grain boundaries of a polycrystalline film.[29,30] Therefore, inhibiting the formation of small crystals eliminates

Table 1. Photovoltaic parameters of best devices with and without MAF: open-circuit voltage (V_{oc}), short circuit current (J_{sc}), fill factor (FF), power conversion efficiency as extracted from the J–V curves (PCE, backward and forward scan) and from the stabilized maximum power point (Stab. PCE) after 60 s of the champion devices in Figure 5 and the average values of each parameter collected by backward scan from seven devices of both control and MAF, respectively.

		Champion devices				Average of seven devices			
	Scan direction	J_{sc} [mA cm⁻²]	V_{oc} [V]	FF	PCE [%]	Stabilized PCE [%]	J_{sc} [mA cm⁻²]	V_{oc} [V]	FF	PCE [%]
Control	Backward	21.7	1.16	0.72	19.1	18.9	21.2 ± 0.7	1.15 ± 0.01	0.72 ± 0.01	18.0 ± 0.8
	Forward	21.7	1.15	0.69	18.1					
MAF	Backward	22.7	1.14	0.71	19.5	19.5	21.7 ± 0.8	1.16 ± 0.02	0.72 ± 0.02	18.8 ± 0.6
	Forward	22.7	1.13	0.69	18.6					

www.MaterialsViews.com

**ADVANCED
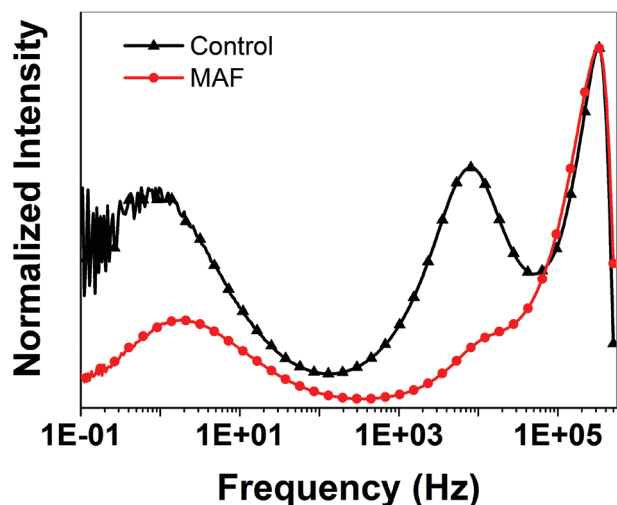ENERGY
MATERIALS**

www.advenergymat.de

COMMUNICATION

Figure 5. Imaginary component frequency spectra of the current response to the light intensity modulated around 100 mW cm^{-2} for devices with and without MAF. The intensities are normalized to the maximum value.

the slow charge transport pathways, which results in better device performances.

In conclusion, we reported planar perovskite solar cells with a record stabilized power conversion efficiency of 19.5%. We demonstrated that controlling the grain size distribution within the perovskite film is crucial to improve the state-of-the-art device. We made use of a specific ionic liquid, methylammonium formate, to retard the perovskite crystal growth in order to form a compact layer with larger grain sizes. XRD and SEM analyses showed that MAF induces larger crystals in the plane of the substrate. Planar perovskite solar cells prepared with MAF exhibited more effective charge transport, which results in higher power conversion efficiency compared to the state-of-the-art devices. Using ionic liquids to control the morphology of the perovskite film is a simple, general, and effective method to enhance the efficiency of planar perovskite solar cells. Further advances are expected from using other ionic liquids that can selectively interact with the different elements composing the perovskite crystals.

Experimental Section

Chemicals and Reagents: All reagents except methylammonium formate and solvents were purchased from commercial sources and used without further purification unless otherwise noted.

Chemical Characterization: ^{1}H NMR spectra were obtained using a Bruker spectrometer (400 MHz) was reported in ppm using DMSO-d as an internal standard. X-ray diffraction (XRD) diagrams were recorded on an X'Pert MPD PRO (Panalytical) equipped with a ceramic tube (Cu anode, $\lambda = 1.54060$ Å), a secondary graphite (002) monochromator, and a real time multiple strip (RTMS) X'Celerator (Panalytical) in an angle range of $2\theta = 10°$ to 40°.

Methylammnonium Formate: MAF was synthesized using a previously reported procedure.[17] $CH_3NH_3(HCOO)$ was synthesized by dropping slowly 6 mL of formic acid (88 wt% in water) in methanol to a solution of 20 mL methylamine (40 wt% in water) in 10 mL absolute ethanol cooled at 0 °C. After mixing reagent, the solution was further stirred for 1 h at 0 °C under vacuum. Then the solution dried at room temperature

under vacuum for 2 d. ^{1}H NMR (400 MHz, DMSO-d): 2.30 (s, 3H), 8.40 (s, 1H) 8.64 (s, 3H).

Solar Cells Fabrication: Devices were fabricated on FTO-coated glass substrates. The substrates were cleaned sequentially with Hellmanex in ultrasonic bath for 30 min, then washed with acetone, isopropanol, and finally cleaned with oxygen plasma for 5 min. Electron selective layer preparation F:SnO$_2$ substrates were cleaned first with acetone, then for 10 min in piranha solution (H$_2$SO$_4$/H$_2$O$_2$ 3: 1 v:v) and then for 10 min in a plasma cleaner prior to atomic layer deposition (ALD). SnO$_2$ was deposited at 118 °C using tetrakis(dimethylamino)- tin(IV) (TDMASn, 99.99%-Sn, Strem Chemicals INC) and ozone at a constant growth rate of 0.065 nm per cycle measured by ellipsometry. TDMASn was held at 65 °C. Ozone was produced using an ozone generator (AC-2025, IN USA Incorporated) fed with oxygen gas (99.9995% pure, Carbagas) producing a concentration of 13% ozone in oxygen. Nitrogen was used as a carrier gas (99.9999% pure, Carbagas) with a flow rate of 10 sccm., before perovskite deposition, the pre-made ALD layers were treated with UV ozone for 10 min to remove byproducts from the deposition process. The perovskite films were deposited from a precursor solution containing MAI(1.1 M, Dysol) and PbI$_2$(1.1 M, TCI Chemicals) in anhydrous DMSO (Acros) for MAPbI$_3$, FAI (1.1 M, Dyesol), PbI$_2$ (1.2 M, TCI Chemicals), MABr (0.2 M, Dyesol), and PbBr$_2$ (0.2 M, TCI Chemicals) in anhydrous DMF:DMSO 4 : 1 (v/v, Acros) for mixed perovskite. Then home-made MAF was added to perovskite solution as the amount, 5 mol% of perovskite. The spin coating program includes two steps, first 1000 rpm for 10 s with a ramp of 200 rpm s^{-1}, then 6000 rpm for 30 s with a ramp of 2000 rpm s^{-1}. 15 s before the end of the spin-coating program, chlorobenzene was gently dropped on the spinning substrate. The substrate was then heated at 100 °C for 1 h on a hotplate in the nitrogen-filled glovebox. The hole transporting material (HTM) was subsequently deposited on the top of the perovskite layer by spin coating from solution at 4000 rpm for 20 s with a ramp of 2000 rpm s^{-1}. The HTM solution was prepared by dissolving the compounds (spiro-OMeTAD) in chlorobenzene at concentration of 70×10^{-3} M, with the addition of 50 mol% of bis(trifluoromethanesulfonyl) imide (Aldrich) from a stock solution of 1.8 M in acetonitrile, 330 mol% of tert-butylpyridine (Aldrich), and 3 mol% of Tris(2-(1H-pyrazol-1-yl)-4-tert-butylpyridine)- cobalt(III) Tris(bis(trifluoromethylsulfonyl)imide) (Dyesol) from a stock solution 0.25 M in acetonitrile. Finally, 80 nm gold layer was deposited by thermal evaporation under high vacuum, using a shadow masking to pattern the electrodes.

Perovskite Film Characterization: A ZEISS Merlin HR-SEM was used to characterize the morphology of the device top view and cross-section. X-ray diffraction (XRD) diagrams were recorded on an X'Pert MPD PRO (Panalytical) equipped with a ceramic tube (Cu anode, $\lambda = 1.54060$ Å), a secondary graphite (002) monochromator, and an RTMS X'Celerator (Panalytical) in an angle range of $2\theta = 10°$ to 40°. Absorption spectral measurements were recorded using Varian Cary5 UV–visible spectrophotometer. Photoluminescence spectra were obtained with Florolog 322 (Horiba Jobin Ybon Ltd.) with the range of wavelength from 620 to 850 nm by exciting at 460 nm. The samples were mounted at 60° and the emission recorded at 90° from the incident beam path. Time-correlated single-photon counting (TCSPC) measurement of perovskite films for fluorescence lifetime data was collected over an area of 26.36 × 26.36 mm^2 using a confocal laser scanning microscope Leica TCS SP8 (63×/1.40). A 440 nm diode laser (1.25 MHz repetition rate) was used for excitation, and a hybrid detector for single molecule detection was used for collection of photons emitted between 700 and 800 nm. A TCSPC module (PicoHarp 300 from PicoQuant) was used to analyze the number of photons as a function of time, as they arrived at the detector. For NMR analysis, the mixed perovskite films with/without MAF sintered at 100 °C were rinsed with butanol for 1 min in the gloves box after cooling down at 25 °C to remove residual MAF and then dried on hotplate 100 °C to evaporate solvent. Dried film was scratched to powder, which was dissolving in D$_2$O.

Solar Cell Characterization: Current–voltage characteristics were recorded by applying an external potential bias to the cell while recording the generated photocurrent with a digital source meter (Keithley Model 2400). The light source was a 450 W xenon lamp

ADVANCED
ENERGY
MATERIALS
www.advenergymat.de

COMMUNICATION

www.MaterialsViews.com

(Oriel) equipped with a SchottK113 Tempax sunlight filter (Praezisions Glas & Optik GmbH) to match the emission spectrum of the lamp to the AM1.5G standard. Before each measurement, the exact light intensity was determined using a calibrated Si reference diode equipped with an infrared cut-off filter (KG-3, Schott). The scan rate was 10 mV s^{-1}. Maximum power point tracking was performed with Keithley model 2400 driven by a homemade algorithm developed in Igorpro software. The cell was initially biased at 1 V. The bias voltage was decreased of 5 mV each 500 ms toward the maximum power point. For each voltage step the algorithm evaluated if the derivative of the power over the time was positive or negative. If the derivative was positive the scan direction remained the same. On the contrary the algorithm changed direction if the derivative was negative. When the bias voltage reached the maximum power point the applied bias oscillated within 10–15 mV perturbing and observing continuously the solar cell under illumination. IPCE spectra were recorded as functions of wavelength under a constant white light bias of ≈10 mW cm^{-2} supplied by an array of white light emitting diodes. The excitation beam coming from a 300 W xenon lamp (ILC Technology) was focused through a Gemini-180 double monochromator (Jobin Yvon Ltd.) and chopped at ≈2 Hz. The signal was recorded using a Model SR830 DSP Lock-In Amplifier (Stanford Research Systems). All measurements were conducted using a nonreflective metal aperture of 0.16 cm^2 to define the active area of the device and avoid light scattering through the sides. Intensity-modulated photocurrent spectroscopy was performed using Autolab PGSTAT302N according to procedures previously reported.[26]

Supporting Information

Supporting Information is available from the Wiley Online Library or from the author.

[1] A. Kojima, K. Teshima, Y. Shirai, T. Miyasaka, *J. Am. Chem. Soc.* **2009**, *131*, 6050.

[2] M. M. Lee, J. Teuscher, T. Miyasaka, T. N. Murakami, H. J. Snaith, *Science* **2012**, *338*, 643.

[3] N. J. Jeon, J. H. Noh, W. S. Yang, Y. C. Kim, S. Ryu, J. Seo, S. I. Seok, *Nature* **2015**, *517*, 476.

[4] National Renewable Energy Laboratory(NREL), http://www.nrel.gov/ncpv/images/efficiency_chart.jpg (accessed: April 2016).

[5] B. P. Fingerhut, W. Zinth, R. de Vivie-Riedle, *Phys. Chem. Chem. Phys.* **2010**, *12*, 422.

[6] Z. L. Ku, Y. G. Rong, M. Xu, T. F. Liu, H. W. Han, *Sci. Rep.-UK* **2013**, *3*, 3132.

[7] S. Albrecht, M. Saliba, J. P. C. Baena, F. Lang, L. Kegelmann, M. Mews, L. Steier, A. Abate, J. Rappich, L. Korte, R. Schlatmann, M. K. Nazeeruddin, A. Hagfeldt, M. Gratzel, B. Rech, *Energy Environ. Sci.* **2016**, *9*, 81.

[8] H. J. Snaith, A. Abate, J. M. Ball, G. E. Eperon, T. Leijtens, N. K. Noel, S. D. Stranks, J. T. W. Wang, K. Wojciechowski, W. Zhang, *J. Phys. Chem. Lett.* **2014**, *5*, 1511.

[9] C. S. Ponseca, T. J. Savenije, M. Abdellah, K. B. Zheng, A. Yartsev, T. Pascher, T. Harlang, P. Chabera, T. Pullerits, A. Stepanov, J. P. Wolf, V. Sundstrom, *J. Am. Chem. Soc.* **2014**, *136*, 5189.

[10] W. S. Yang, J. H. Noh, N. J. Jeon, Y. C. Kim, S. Ryu, J. Seo, S. I. Seok, *Science* **2015**, *348*, 1234.

[11] Q. Chen, H. P. Zhou, Z. R. Hong, S. Luo, H. S. Duan, H. H. Wang, Y. S. Liu, G. Li, Y. Yang, *J. Am. Chem. Soc.* **2014**, *136*, 622.

[12] F. Z. Huang, Y. Dkhissi, W. C. Huang, M. D. Xiao, I. Benesperi, S. Rubanov, Y. Zhu, X. F. Lin, L. C. Jiang, Y. C. Zhou, A. Gray-Weale, J. Etheridge, C. R. McNeill, R. A. Caruso, U. Bach, L. Spiccia, Y. B. Cheng, *Nano Energy* **2014**, *10*, 10.

[13] D. Bi, W. Tress, M. I. Dar, P. Gao, J. Luo, C. Renevier, K. Schenk, A. Abate, F. Giordano, J. P. Correa Baena, J. D. Decoppet, S. M. Zakeeruddin, M. K. Nazeeruddin, M. Gratzel, A. Hagfeldt, *Sci. Adv.* **2016**, *2*, e1501170.

[14] P. W. Liang, C. Y. Liao, C. C. Chueh, F. Zuo, S. T. Williams, X. K. Xin, J. Lin, A. K. Jen, *Adv. Mater.* **2014**, *26*, 3748.

[15] D. T. Moore, K. W. Tan, H. Sai, K. P. Barteau, U. Wiesner, L. A. Estroff, *Chem. Mater.* **2015**, *27*, 3197.

[16] M. Shahiduzzaman, K. Yamamoto, Y. Furumoto, T. Kuwabara, K. Takahashi, T. Taima, *RSC Adv.* **2015**, *5*, 77495.

[17] J. P. Belieres, C. A. Angell, *J. Phys. Chem. B* **2007**, *111*, 4926.

[18] J. Catalano, A. Murphy, Y. Yao, G. P. A. Yap, N. Zumbulyadis, S. A. Centeno, C. Dybowski, *Dalton T.* **2015**, *44*, 2340.

[19] N. J. Jeon, J. H. Noh, Y. C. Kim, W. S. Yang, S. Ryu, S. Il Seol, *Nat. Mater.* **2014**, *13*, 897.

[20] F. Holtzberg, B. Post, I. Fankuchen, *J. Chem. Phys.* **1952**, *20*, 198.

[21] I. M. Hermes, S. A. Bretschneider, V. W. Bergmann, D. Li, A. Klasen, J. Mars, W. Tremel, F. Laquai, H. J. Butt, M. Mezger, R. Berger, B. J. Rodriguez, S. A. L. Weber, *J. Phys. Chem. C* **2016**, *120*, 5724.

[22] J. P. C. Baena, L. Steier, W. Tress, M. Saliba, S. Neutzner, T. Matsui, F. Giordano, T. J. Jacobsson, A. R. S. Kandada, S. M. Zakeeruddin, A. Petrozza, A. Abate, M. K. Nazeeruddin, M. Gratzel, A. Hagfeldt, *Energy Environ. Sci.* **2015**, *8*, 2928.

[23] J. W. Lee, T. Y. Lee, P. J. Yoo, M. Gratzel, S. Mhaisalkar, N. G. Park, *J. Mater. Chem. A* **2014**, *2*, 9251.

[24] J. H. Heo, M. H. Lee, H. J. Han, B. R. Patil, J. S. Yu, S. H. Im, *J. Mater. Chem. A* **2016**, *4*, 1572.

[25] Y. Shao, Y. Yuan, J. Huang, *Nat. Energy* **2016**, *1*, 15001.

[26] K. Zhu, N. Kopidakis, N. R. Neale, J. van de Lagemaat, A. J. Frank, *J. Phys. Chem. B* **2006**, *110*, 25174.

[27] J. P. C. Baena, M. Anaya, G. Lozano, *Adv. Mater.* **2016**, *28*, 5031.

[28] F. Giordano, A. Abate, J. P. Correa Baena, M. Saliba, T. Matsui, S. H. Im, S. M. Zakeeruddin, M. K. Nazeeruddin, A. Hagfeldt, M. Graetzel, *Nat. Commun.* **2016**, *7*, 10379.

[29] W. Zhang, M. Saliba, D. T. Moore, S. K. Pathak, M. T. Horantner, T. Stergiopoulos, S. D. Stranks, G. E. Eperon, J. A. Alexander-Webber, A. Abate, A. Sadhanala, S. Yao, Y. Chen, R. H. Friend, L. A. Estroff, U. Wiesner, H. J. Snaith, *Nat. Commun.* **2015**, *6*, 6142.

[30] J. H. Im, I. H. Jang, N. Pellet, M. Gratzel, N. G. Park, *Nat. Nanotechnol.* **2014**, *9*, 927.